Bioactive Materials 6 (2021) 1765–1776

Contents lists available at ScienceDirect

Bioactive Materials

journal homepage: www.sciencedirect.com/journal/bioactive-materials

The effect of different coatings on bone response and degradation behavior of porous magnesium-strontium devices in segmental defect regeneration

Nan Zhang [a,d,1], Weidan Wang [b,c,1], Xiuzhi Zhang [b], Krishna. C. Nune [e], Ying Zhao [f], Na Liu [a], R. D.K. Misra [e], Ke Yang [c,***], Lili Tan [c,**], Jinglong Yan [d,*]

[a] Department of Orthopedic Surgery, The 2nd Affiliated Hospital of Qiqihar Medical University, Qiqihar, 161000, China
[b] Department of Orthopaedics, Affiliated Zhongshan Hospital of Dalian University, Dalian, 116001, China
[c] Institute of Metal Research, Chinese Academy of Sciences, Shenyang, 110016, China
[d] Department of Orthopedic Surgery, The 2nd Affiliated Hospital of Harbin Medical University, Harbin, 150081, China
[e] Department of Metallurgical, Material and Biomedical Engineering, The University of Texas at EI Paso, TX, 79968, USA
[f] Shenzhen Institutes of Advanced Technology, Chinese Academy of Sciences, Shenzhen, 518055, China

ARTICLE INFO

Keywords:
Magnesium-strontium alloy
Segmental defect
Degradation behavior
Bone regeneration

ABSTRACT

Regeneration of long-bone segmental defects remains a challenge for orthopedic surgery. Current treatment options often require several revision procedures to maintain acceptable alignment and achieve osseous healing. A novel hollow tubular system utilizing magnesium-strontium (Mg–Sr) alloy with autogenous morselized bone filled inside to repair segmental defects was developed. To improve the corrosion and biocompatible properties, two coatings, Ca–P and Sr–P coatings, were prepared on surface of the implants. Feasibility of applying these coated implants was systematically evaluated *in vitro* and *in vivo,* and simultaneously to have a better understanding on the relationship of degradation and bone regeneration on the healing process. According to the *in vitro* corrosion study by electrochemical measurements, greater corrosion resistance was obtained for Ca–P coated sample, and attributed to the double-layer protective structure. The cytotoxicity and alkaline phosphatase (ALP) assays demonstrated enhanced bioactivity for Sr–P coated group because of the long-lasting release of beneficial Sr^{2+}. At 12 weeks post-implantation with Mg–Sr alloy porous device, the segmental defects were effectively repaired with respect to both integrity and continuity. In addition, compared with the Ca–P coated implant, the Sr–P coated implant was more proficient at promoting bone formation and mineralization. In summary, the Sr–P coated implants have bioactive properties and exceptional durability, and promote bone healing that is close to the natural rate, implying their potential application for the regeneration of segmental defects.

1. Introduction

Fracture non-unions and large bone defects, caused by severe trauma, infection, congenital malformation or malignance, etc. Continue to be clinically challenging. Autologous and allogeneic bone grafts are widely used treatment modalities [1]. However, these techniques have a number of drawbacks, including restricted availability, donor-site morbidity for autografts, bone graft resorption, and immunological rejection for allografts. In response, there is increasing demand for developing new and efficient treatment practices. Encouraging successful bone defects regeneration is a complex task requiring harmonious interplay of cells, cellular support scaffolds, bioactive growth factors, and physiological systems in the existing tissue [2,3]. However, the majority of scaffolds that are commonly used for bone reconstruction are usually made from slowly hydrolyzing polymers or ceramics with unpredictable degradation rates and insufficient mechanical strength [4,5]. The disadvantages associated with the use of these scaffolds, include immunogenicity and high cost. In addition, a titanium (Ti) mesh with

* Corresponding author.
** Corresponding author.
*** Corresponding author.
E-mail addresses: kyang@imr.ac.cn (K. Yang), lltan@imr.ac.cn (L. Tan), yjlg4@aliyun.com (J. Yan).
[1] , These authors contributed equally to this work.

https://doi.org/10.1016/j.bioactmat.2020.11.026
Received 27 June 2020; Received in revised form 10 November 2020; Accepted 17 November 2020

morselized bone was used to therapy large segmental defect, which can play a supporting and protective role to avoid bone graft to be resorbed and removed [6]. However, titanium does not degrade *in vivo*, it will persist in the body and is difficult to remove — especially after the bone defect has recovered. Meanwhile, the long-term presence of Ti mesh may cause complications, such as secondary bone absorption, stress shielding and the high risk of re-fractures [7,8]. Therefore, it is necessary to study degradable and more suitable material for treating this serious disease.

In the past decade, biodegradable magnesium (Mg) alloys have emerged as promising biomaterials for next-generation biomedical devices. First of all, the released Mg ions derived from degradation are non-toxic, because Mg is the fourth most abundant element in the human body, and it is essential for regulation of muscle contraction and metabolism [9], thus Mg alloys has superior biocompatibility. Moreover, the mechanical strength, elastic modulus and density of Mg alloys closely match the natural bone, which helps to reduce postoperative stress shielding or stress concentration. More importantly, Mg alloys degrade in a biological environment, thereby obviating the need for a second surgery to remove a device. In addition, *in vitro* and *in vivo* studies also indicated that released Mg ions may promote new bone formation and increased expression of osteogenic markers [10,11], and may enhance the mineralization of Ca^{2+} surrounding the implant [12], and may accelerate osteogenesis and osseointegration [13]. All these characteristics indicate that Mg alloy has great advantages as a biomaterial for repairing bone defect. However, Mg alloy has poor corrosion resistance in the body because it will degraded to produce $Mg(OH)_2$ and H_2 in aqueous environments [8–10,12,13], which can greatly reduce the mechanical strength and fatigue life of Mg-base implants in the body. Therefore, this also was a major obstacle to their clinical applications.

We considered the selection of alloy elements for Mg and the coating method, with the goal of achieving more perfect corrosion resistance and a microenvironment that accelerates new bone formation. In previous study, we had developed magnesium-strontium (Mg–Sr) alloy as a biodegradable substitute for bone [14,15], as Sr can upregulate the proliferation osteoblasts and hence support new bone formation by increased matrix synthesis through the calcium-sensing receptor and ERK signal pathway [16,17]. Sr can also decrease bone resorption by inhibiting osteoclast activity through increasing the expression of osteopontin (OPN) and decreasing the expression of receptor activator of nuclear factor kappa B ligand (RANKL) [18–20]. Furthermore, Sr can provide precipitation strengthening and enhance the mechanical properties of the Mg matrix [10]. However, the surface of Mg–Sr alloy is highly reactive in the physiological environment containing chloride, and thus the surface may become pitted owing to the micro-galvanic effect between the second phase and Mg matrix. These characteristics limited the further clinical application of Mg–Sr alloy as a biomaterial.

Therefore, different surface modification methods have been attempted for enhancing the corrosion resistance and biocompatibility. In present study, two surface modification methods were used on Mg–Sr alloy device: a Sr–P chemical conversion coating (Sr–P) and Ca–P deposition coating (Ca–P). Sr–P coating was selected as a bio-functional coating supplemented with Sr, with the goal of providing sustained release of bioactive Sr^{2+}, which can promote the osteogenic differentiation of MSCs by upregulating the expression of osteoblast marker genes, such as Runx 2, OCN, OPN, bone sialoprotein (BSP), as well as type 1 collagen, and increases ALP activity and matrix mineralization [20,21]. On the other hand, the Ca–P coating enhanced corrosion resistance and improved biocompatibility because the primary composition is brushite ($CaHPO_4{\cdot}2H_2O$) [22]. Released Ca^{2+} also can promotes the proliferation of mesenchymal precursor cells, as well as mature bone cells nitric oxide–dependent process (NO) [2]. Thus, the effect of two coatings on the degradation behavior and biological property of Mg–Sr alloy was further studied *in vitro*. In addition, we fabricated Mg–Sr porous device with two coating, and the corresponding effect on segmental defect regeneration was studied in the critical-size ulna defect of New Zealand rabbits up to 3 months.

2. Materials and methods

2.1. Materials and preparation of samples

The Mg-1.5Sr alloys were fabricated by melting down pure Mg (99.95 wt%) and Mg–25Sr master alloy, with subsequent extrusion at 350 °C and extrusion ratio of 64:1. Its composition was confirmed by ICP (Inductively Coupled Plasma) as 1.5 wt% Sr, <0.001 wt% Fe, <0.001 wt % Ni, and Mg in balance. Disc samples of Φ10 mm × 3 mm were used for *in vitro* study. Tubular-shaped hollow Mg–Sr alloy device with Φ4 mm in outer diameter, 0.5 mm in wall thickness and 15 mm in length were fabricated for the animal tests.

Mg–Sr samples were coated with Sr–P via a one-step conversion process by immersion in a solution containing 0.1 M Sr $(NO_3)_2$ and 0.06 M $NH_4H_2PO_4$ at 80°Cfor 10 min, with pH being adjusted to 3.0 with diluting HNO_3. Other Mg–Sr samples were coated with Ca–P in two steps: fluorination with aqueous 0.1 M kF at 20 °C for 24 h, then immersion in a mixed solution of $NaNO_3$, Ca $(H_2PO_4)_2{\cdot}H_2O$ and H_2O_2 at 20 °C for 24 h. All the samples were roughened with silicon-carbon grinding paper 2000 grit, followed by ultrasonically cleaning with acetone, absolute ethanol, distilled water and dried in air. All devices were sterilized with ethylene oxide prior to implantation.

2.2. Characterization of samples

The surface and cross-section morphologies, thickness, and elemental composition of Sr–P coated and Ca–P coated samples was studied by scanning electron microscopy (SEM, S–3400 N, Hitachi, Japan), equipped with energy-dispersive spectroscopy (EDS). The cross-section of bare Mg–Sr alloy and each coated sample was assessed after imbedding in polymethyl methacrylate (PMMA) and dried for 24 h in air. Next, the samples were ground, polished and sputter-coated with a thin layer of gold for conductivity.

2.3. In vitro tests

2.3.1. Electrochemical test

Electrochemical corrosion behavior of coated samples in Hank's solution at 37 ± 0.5 °C was studied using an electrochemical workstation (Reference 60, Gamry, USA). A three-electrode cell, using platinum as the counter-electrode and a saturated calomel electrode (SCE) as the reference electrode, was employed for electrochemical measurements. First, open circuit potential (OCP) curves were obtained for 30 min. Next, electrochemical impedance spectroscopy (EIS) was performed on the same sample, with AC voltage of 10 mV rms and in the frequency range of 100 kHz to 0.01 Hz. The corrosion performance by EIS of all the systems was studied at open circuit potential (OCP). The potentiodynamic polarization was carried out in the end, at a scanning rate of 0.5 mV s^{-1} with an initial potential of −250 mV *versus* OCP. The EIS results were fitted by ZSimpWin 3.10 software. An average of three measurements was obtained for each group.

2.3.2. Immersion test

To further test the long-term durability of the Mg–Sr samples *in vitro*, pH variation and weight loss were measured after 28 days of immersion in Hank's solution at 37 °C, with an immersion ratio of 1.25 cm^2/mL. The immersion media was changed every day. and the pH value was recorded every day during the early stage and after one day interval until 14 days. At 7, 14 and 28 days, chromic acid solution (200 g/L CrO_3 and 10 g/L $AgNO_3$) was added to remove the corrosion products and the remaining coating in the ultrasonic bath for 15 min.

2.3.3. Osteogenic differentiation assays

The bone mesenchymal stem cells of rabbit (RBMSC) were cultured

in Dulbecco's modified Eagle media (DMEM) containing 10% fetal bovine serum (FBS) at 37 °C under a humidified atmosphere of 5% CO_2 environment. CCK-8 assay was used to evaluate the cytotoxicity of the bare Mg–Sr alloy and coated samples. Both indirect contact method (sample extracts) and direct contact method were conducted for studying the effect of ions release and bioactivity of the coated samples, respectively. In the indirect contact method, extracts of the samples were prepared using a ratio of sample surface area to solution volume at 1.25 cm^2/mL for 24 h according to ISO 10993–5 [23]. Cells were seeded at a density of 4 × 10^4 cells/mL, and incubated for 24 h to allow attachment. Next, the culture medium was replaced with sample extracts and incubated for 1, 3 and 5 days. The medium or supplemented extracts were refreshed every two days as regular intervals. As regards the direct contact method, passage cells in logarithmic growth phase were rinsed with PBS, and counted to 20,000 cells/cm^2 after trypsinization, incubated on the surface of samples in a sterile 24-well plate for direct contact, and cultured for identical time. 10% of the total medium volume with cell counting kit-8 (CCK-8) reagent (Dojindo Molecular Technologies, Inc., Kumamoto, Japan) was added in each well, and then incubated for 2 h at 37 °C. The absorbance was read at 450 nm to measure the optical density value (OD).

ALP staining was performed to evaluate osteogenic activity and was determined using a BCIP/NBT ALP color development kit (Beyotime Institute of Biotechnology, Haimen, China). Following incubation for 7 days at 37 °C, RBMSCs were washed with PBS twice and fixed in 4% paraformaldehyde (PFA) for 10 min at room temperature. Then washed with deionized water twice and incubated cells with for 1 h, 37 °C and washed with deionized water twice. Images were then acquired using a phase contrast microscope equipped with a charge-coupled device (CCD) camera. Image-Pro Plus 6.0 (Media Cybernetics, Inc., Rockville, MD, USA) was used to evaluate the percentage of the total stained area.

Alizarin red S forms a chelate complex with the calcium ion, was used to analyze calcium salts in cells and tissues. RBMSCs (5 × 10^4 cells/well) were cultured in a 6-well plate and treated with extract of two coated and uncoated alloys for 21 days at 37 °C. Negative control cells were regularly cultured with the same time. The cells were fixed in 4% PFA for 10 min after washing with PBS, and the fixed cells were stained with 1% (w/v) Alizarin red at pH 4.4 for 1 h. Then, samples were thoroughly rinsed with deionized water and images were acquired and evaluated as described in ALP staining.

2.4. In vivo tests

2.4.1. Surgery

Animal tests were approved by the Institutional Animal Care and Use Committee of Harbin Medical University. 54 pathogen-free adult New Zealand white rabbits (2.6 ± 0.3 kg) were randomly assigned to three groups (n = 18), including Sr–P coated porous device (Sr–P coating group), Ca–P coated porous device (Ca–P coating group) and autogenous morselized bones (control group). The rabbits were anesthetized intravenously through their ear veins with 3% (w/v) pentobarbital sodium (30 mg/kg). Firstly, the iliac bone was harvested from each animal, and stripped from the periosteum and cartilage. Secondly, the bone was converted into fine bone powders of diameters 300–500 μm using a spherical grinding drill [24]; Next, both forearms of the rabbits were shaved and disinfected, and each ulna was exposed via dissection. Finally, ulna osteotomies were performed 15 mm apart using an oscillating saw under saline irrigation. Each device was filled with compacted fine autogenous iliac bone powder and carefully placed into the ulna defect position (Fig. 1) [25]. The surrounding soft tissue and muscle were carefully sutured to stabilize the device.

Post-implantation rabbits were housed in an environmentally controlled animal care lab. Each rabbit received a subcutaneous injection of 10 mg/kg penicillin and 0.5 mg/kg lornoxicam for 3 days to prevent infection and relieve pain. Immediately following the surgery, the animals were allowed to resume normal movement, including bearing weight on their forearms. Six rabbits were sacrificed at 4, 8, and 12 weeks after surgery. The bilateral forearms were collected and then frozen at −20 °C for further test.

2.4.2. Radiographic analyses

To monitor the progress of implant degradation and bone healing, radiographs were taken every 4 weeks with an X-ray scanner (Faxitron, USA) at 110 kV and anode current of 500 μA. At design time point, the X-ray images of ulna defect site were assessed and scored from three parts, including bone formation (0–4), union (0–4) and remodeling (0–4) by three independent investigators according to the previously reported method [26], with average of three measurements for each sample. Scores ranged from 0 (no healing) to 12 (restore to normal bone), and 7 score was considered for the defect to be preliminarily reconstructed.

2.4.3. Micro-CT evaluation

The forearms of the rabbits were scanned using a Siemens Inveon Micro-CT system (Siemens Medical Solutions, Germany). Three-dimensional (3D) images of the defect were generated from the acquired 2D lateral projections using Inveon software. Implants could be discerned from the surrounding soft and hard tissues based on their absorption coefficient (equivalent to mineral density). The residual volume was determined by 3D morphometric analysis, and the corresponding corrosion rate was calculated according to the following equation [27].

$$CR = \Delta V/(At) \quad (1)$$

where CR is the corrosion rate (mm/year), ΔV is the absolute volume-loss value of device (mm^3), A is the surface area of porous device (mm^2), and t is the implantation time (year).

2.4.4. Calcein fluorescence

To characterize the mineralization of newly formed bone, a solution of 1% (w/v) calcein in 2% (w/v) $NaHCO_3$ (10 mg/kg, Sigma-Aldrich, USA) was injected subcutaneously at 3 days before sacrifice the animal. Then ulna was harvested and fixed in 75% (v/v) ethanol. The samples were embedded in polymethyl methacrylate (PMMA) and cut into sections of ~120 μm using an EXAKT/E300CP microtome (Leica, Germany). The uncalcified sections were polished to a thickness of ~50 μm for imaging by a DM4000B fluorescent microscope (Leica, Germany). Subsequently, the Image-J software (National Institutes of Health, USA) was used to calculate the area of the newly formed bone.

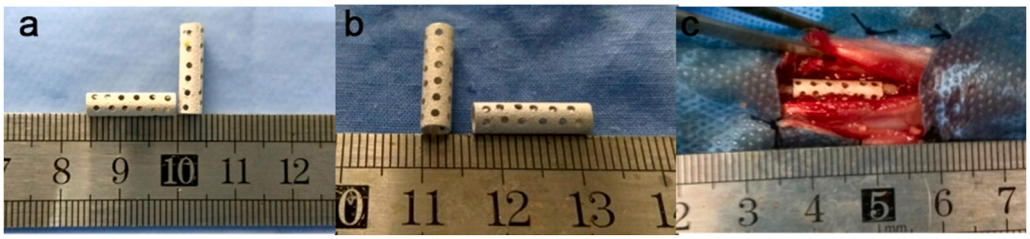

Fig. 1. Ca–P coated (a) and Sr–P coated (b) Mg–Sr alloy porous devices used in the *in vivo* test. (c) Implantation of the coated Mg–Sr device in a rabbit ulna defect.

To improve the calculation accuracy and reduce the artificial error, five different sites were selected in each image. Four sites were randomly selected proximal and distal between the implant and the bone, and a fifth site was selected from the middle outside part of the defect site. Then, the average area of new bone formation at these five sites were calculated.

2.4.5. Histology

Ulna samples were sectioned as described in Section 2.4.4, followed by staining with Van Gieson's picrofuchsin solution (Sigma-Aldrich, USA) to visualize osteocytes, chondrocytes and the surrounding soft tissues. The sections were observed and photographed using an Olympus ×71 optical microscope (Olympus, Japan).

2.4.6. Statistical analysis

Statistical analysis was performed using SAS 9.4 software (Statistical Analysis System, USA). All the results are the mean ± the standard deviation. All the data were analyzed via Wilcoxon test. Values of $p < 0.05$ indicated statistical significant.

3. Results

3.1. Characterization of coatings

Fig. 2 (a)-(d) shows the surface and cross-sectional SEM micrographs of Sr–P and Ca–P coatings on Mg–Sr alloy. The Sr–P surface comprised highly crystallized, prismatic particles, and the coating thickness was ~10 μm. The Ca–P surface had petal-shaped particles, and the coating thickness was ~25 μm. Moreover, a double-layer structure appeared from the cross-sectional image of Ca–P coated samples. According to the results of energy dispersive X-ray spectroscopy (EDS) in Fig. 2 (e, f), Mg and F were detected in the inner layer of Ca–P coating, implying the presence of MgF_2. Meanwhile the outer layer showed an atomic ratio of Ca to P of ~1:1, identical to brushite. As regards Sr–P coating, Sr and P had an atomic ratio of 1:1, besides oxygen.

3.2. Corrosion behavior in vitro

In vitro corrosion behavior of Ca–P coated, Sr–P coated and uncoated Mg–Sr alloy discs were studied based on the electrochemical measurement and immersion test. For the electrochemical test, OCP curves are generally performed first to study the chemical stability of surface and establish conditions for the immersion tests. As shown in Fig. 3a, Ca–P and Sr–P coated samples drifted rapidly to more noble side rapidly and fluctuated within a small range. While the increase potential value in uncoated Mg–Sr disc was caused by the formation of partially protective $Mg(OH)_2$ layer with the dissolution of Mg, which indicated the fact that it was difficult to obtain a stable state in the case of uncoated Mg–Sr alloy during corrosion process. From the thermodynamic perspective, the higher OCP value for each of coated samples implies a more stable electrochemical state than the uncoated Mg–Sr matrix.

Fig. 3b presents the polarization curves of the coated samples immersed in Hank's solution at 37 °C. Table 1 summarizes data for corrosion potential (E_{corr}), corrosion current density (I_{corr}), and corrosion rate (CR) that were derived from these curves. The polarization curves were fitted with Gamry Echem Analyst software and the corrosion current was directly from the polarization plots by extrapolating the Tafel region. Considering the complex anodic reaction that included dissolution of Mg and the formation of corrosion products, the polarization curves were fitted by selecting the linear part of the cathodic curve that commenced 50 mV from the corrosion potential (E_{corr}). Subsequently, the intercept corrosion rate (V_{corr}) and current density (I_{corr}) were calculated from the value where the vertical lines of the selected point intercepted the true Ecorr value, as reported by Jiang

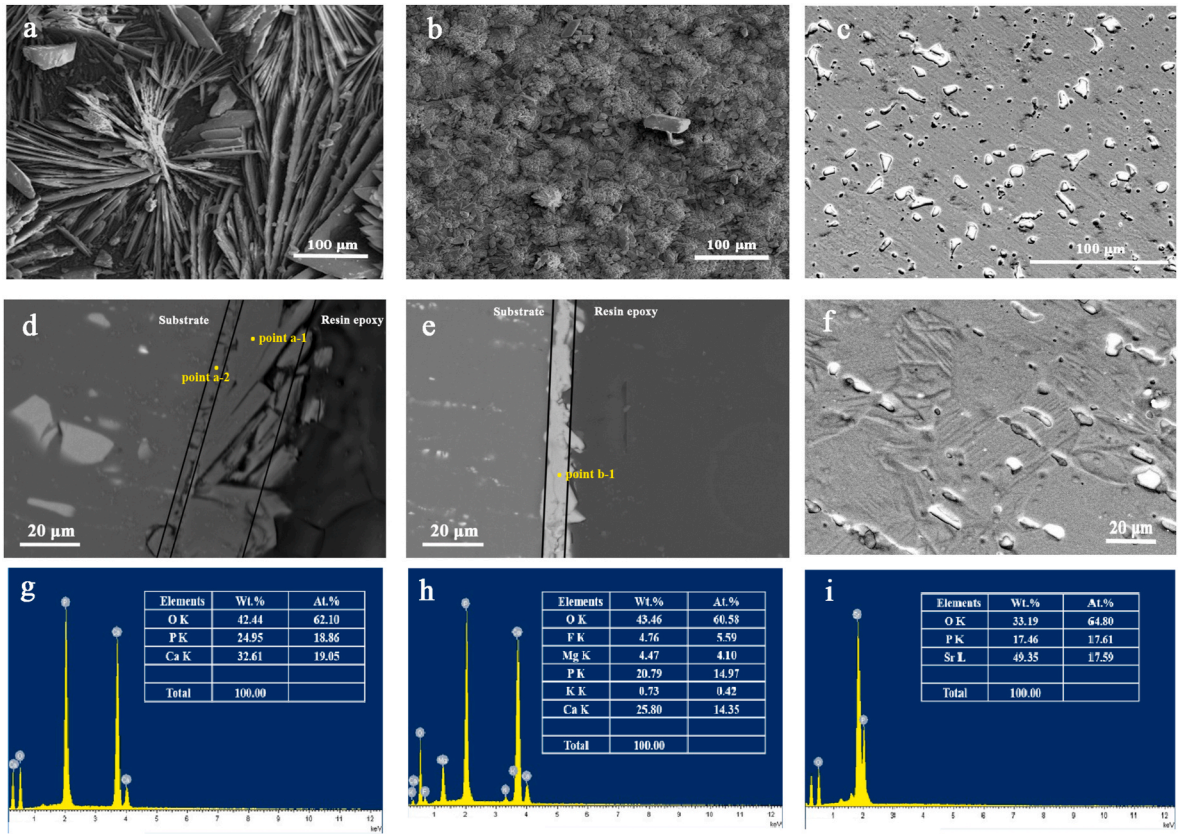

Fig. 2. Characterization of surface and cross-sectional morphologies of Ca–P coating (a, d), Sr–P coating (b, e) and bare Mg–Sr alloy (c, f). EDS results of different positions indicated by "point a1" (g), "point a2" (h), and "point b1" (i).

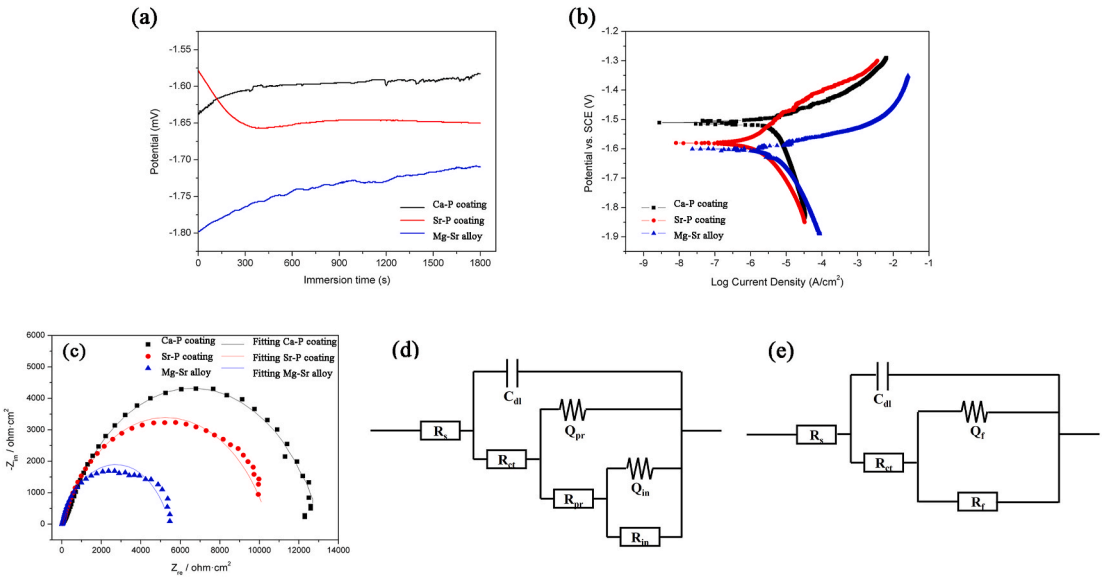

Fig. 3. Electrochemical measurements of Ca–P and Sr–P coated samples in Hank's solution: (a) open circuit potential curves; (b) potentiodynamic polarization plots; (c) Nyquist plots; equivalent circuits of (d) Ca–P coated alloy, (e) Sr–P coated and uncoated alloy for impedance spectra.

Table 1
E_{corr} and I_{corr} values calculated from the potentiodynamic polarization curves of Ca–P, Sr–P coated and uncoated Mg–Sr alloy in Hank's solution, by extrapolating the Tafel region.

Materials	E_{corr} (V)	I_{corr} (μA/cm^2)	V_{corr} (mm/y)
Ca–P coating	−1.52	1.41	0.032
Sr–P coating	−1.59	2.46	0.057
Mg–Sr alloy	−1.60	3.68	0.084

et al. [28–30]. I_{corr} of the Ca–P coated sample (1.41 μA/cm^2) was lower than the Sr–P coated sample (2.46 μA/cm^2), suggesting a lower degradation rate for the former. In addition, the uncoated Mg–Sr alloy exhibited the highest corrosion current density of 3.68 μA/cm^2. Meanwhile, electrochemical impedance spectrum (EIS) was employed to investigate the corrosion characteristics of the two different coatings and uncoated alloys, and Fig. 3c provides the resultant plots and fitted lines. Both coated samples indicated larger diameter than Mg–Sr alloys, which corresponds to OCP and PD results. In the case of coated samples, Ca–P coating exhibited a larger diameter than Sr–P coating, implying superior corrosion resistance. Equivalent circuit models were proposed, as shown in Fig. 3d and e, based on morphology characteristics and structure examinations (Fig. 2). Here R_s is the solution resistance, R_{ct} is the charge transfer resistance of the corrosion process at the solution/coating interface, and C_{dl} is the double layer capacitance. The R_f/CPE_f pair describes the film resistance as well as the film capacity of the outer layer for both coatings, because of the blocking effect to corrosion. While for uncoated alloys, the outer film was $Mg(OH)_2$ layer due to degradation process. In addition, the constant phase element (CPE) was used because of the rough surface. Another R_{pr}/CPE_{pr} pair was applied to the Ca–P coating because of inner pre-treated MgF_2 layer, as noted in the cross-sectional morphology and chemical composition. The resistance values obtained from EIS fitting results of the two coating systems are presented in Table 2. It can be seen that R_f of Sr–P coating was 10,420 Ω cm^2. While the Ca–P coating had R_{pr} of 3650 Ω cm^2, connected with another R_{in} of 12,620 Ω cm^2. An overall enhanced resistance value for the Ca–P coating was obtained compared to Sr–P coating, which is also in accordance with the above potentiodynamic polarization results. The uncoated Mg–Sr alloy had the poorest corrosion resistance with a value of 5417 Ω cm^2.

Given that the electrochemical tests are instantaneous measurements, a long-term, 28-day immersion test was carried to further evaluate corrosion resistance. The pH value is plotted in Fig. 4a. The pH value was higher for the uncoated Mg–Sr alloy than the two coated Mg–Sr alloy, indicating a more severe corrosion without coating. In the first two days, the pH value for the noncoated alloy increased dramatically, after which the pH value fluctuated, as reported previously [31–33]. The relatively high pH value at the beginning was because of the degradation of magnesium in aqueous solution. As the immersion time prolonged, the decrease was caused by the partial coverage of the corrosion products, which slowed further corrosion. Fig. 4b shows weight loss at three time points. It is observed that the uncoated Mg–Sr alloy exhibited greatest weight loss during the entire immersion period. While the lowest corrosion was obtained with Ca–P coated alloy. Moreover, long-term immersion test indicated degradation behavior identical to the electrochemical tests. The sequence was: uncoated Mg–Sr alloy > Sr–P coated alloy > Ca–P coated alloy.

Table 2
Electrochemical data obtained from EIS curves of Ca–P and Sr–P coated Mg–Sr alloy in Hank's solution.

Ca–P coating	R_{ct} (Ω·cm^2)	C_{dl} (S·cm^{-2} s^{-1})	R_{pr} (Ω·cm^2)	Q_{pr} (S·cm^{-2} s^{-1})	n	R_{in} (Ω·cm^2)	Q_{in} (S·cm^{-2} s^{-1})	n
	40.83	1.87×10^{-7}	3650	6.33×10^{-6}	0.75	12,620	9.38×10^{-6}	0.75
Sr–P coating	R_{ct} (Ω·cm^2)	C_{dl} (S·cm^{-2} s^{-1})	R_f (Ω·cm^2)	Q_f (S·cm^{-2} s^{-1})	n			
	33.34	9.51×10^{-8}	10,420	2.97×10^{-5}	0.73			
Mg–Sr alloy	R_{ct} (Ω·cm^2)	C_{dl} (S·cm^{-2} s^{-1})	R_f (Ω·cm^2)	Q_f (S·cm^{-2} s^{-1})	n			
	19.27	1.23×10^{-6}	5417	4.51×10^{-5}	0.77			

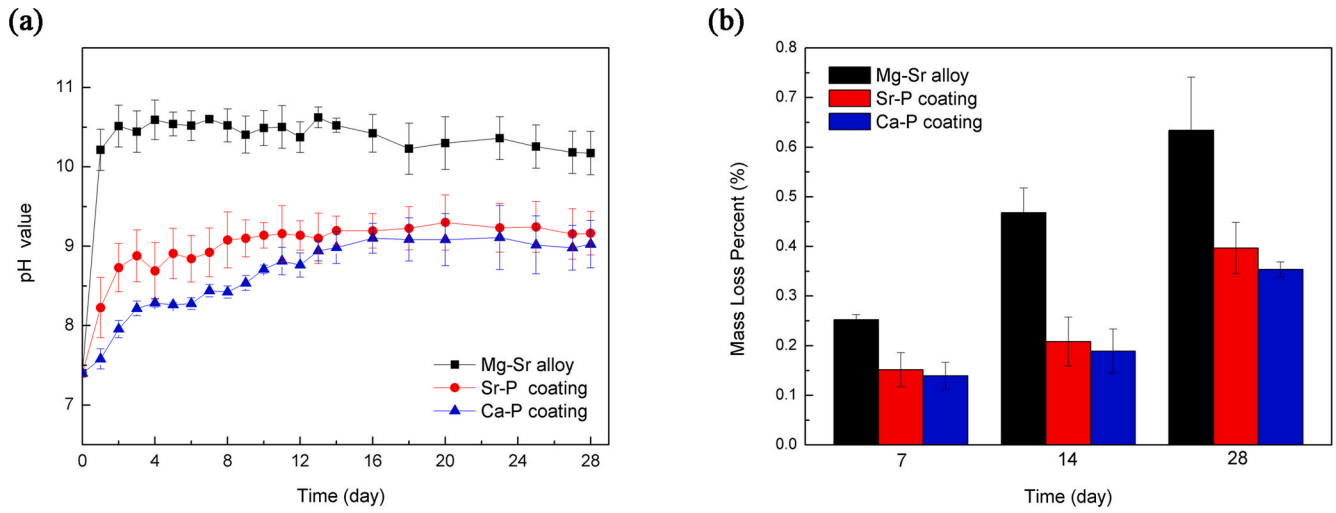

Fig. 4. Long-term immersion test of uncoated Mg–Sr alloy and Ca–P, Sr–P coated alloys in Hank's solution, (a) pH value, (b) weight loss.

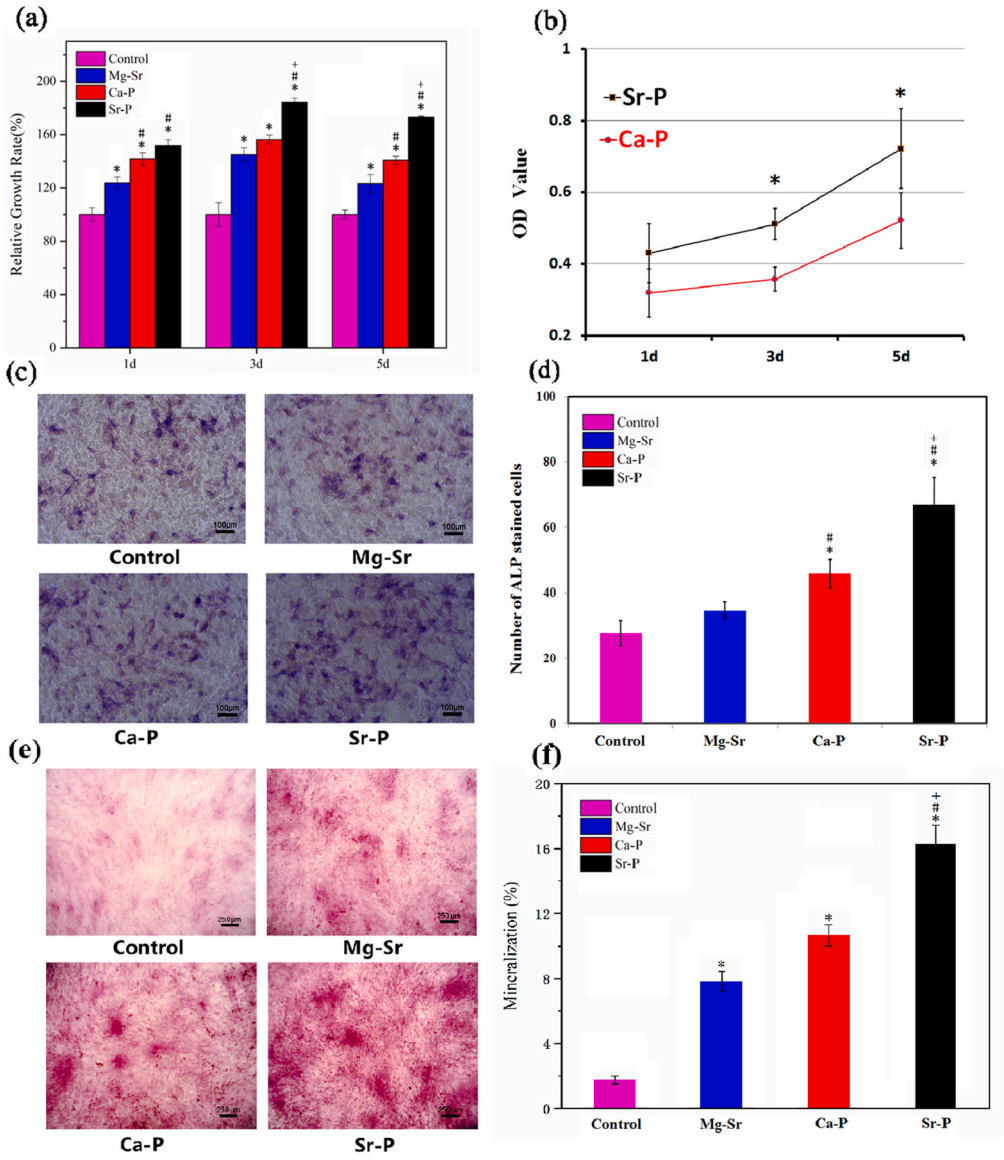

Fig. 5. (a) Viabilities of RBMSC cultured by indirect contact method of coated and uncoated Mg–Sr alloy for 1, 3, 5 days, (b) CCK-8 assay on surfaces of Sr–P and Ca–P coated samples. Staining results and statistical analyses of ALP activities at 7 days with extracts of coated and uncoated Mg–Sr alloy (c, d). Mineralization following treatment of RBMSC with negative control, uncoated and coated alloys for 21 days were identified by Alizarin red S. (e, f). Significantly difference at $p < 0.05$ is shown with different symbols. (*, # and + represent $p < 0.05$ when compared with negative control, bare Mg–Sr alloy and Ca–P coating, respectively). (For interpretation of the references to color in this figure legend, the reader is referred to the Web version of this article.)

3.3. Cell proliferation and alkaline phosphatase activity

The viability of RBMSC cultured in extracts of Mg–Sr alloy samples with and without coating after 1, 3, 5 days are shown in Fig. 5a. Sr–P coating showed highest cell proliferation, while both Sr–P coating and Ca–P coating indicated statistically better biocompatibility than blank control group and bare Mg–Sr alloy. Fig. 5b shows the viability of RBMSC cultured directly on surfaces of Sr–P and Ca–P coated samples. The uncoated alloy underwent severe degradation owing to hydrogen evolution, which was harmful to adhere cells on the surface. Consequently, only two coated samples were studied in the direct contact culturing experiment. Indirect test also demonstrated a higher OD value of Sr–P coating than Ca–P coating samples. Tissue non-specific ALP is an enzyme expressed by cells during osteogenesis [34], therefore, higher ALP activity indicates a better potential osteogenic effect. In the present study, RBMSC were cultured for 7 days with sample extracts of two coated and uncoated alloys (indirect contact). In indirect contact experiment, ALP activity was statistically higher for the Sr–P coating compared with each of the uncoated alloy after 7 days (Fig. 5c and d). Considering Alizarin red S is widely applied as a classical technique to demonstrate mineralization and late osteogenesis [35,36], therefore, RBMSC were cultured for 21 days with sample extracts of two coated and uncoated alloys in order to demonstrate the long-term effect on osteogenesis. The staining images and quantitative results revealed that the degree of mineralization were significantly increased following treatment with Sr–P coating (Fig. 5e and f). Meanwhile, both coated and uncoated alloys significantly promoted the mineralization compared with negative control group after 21 days.

3.4. In vivo study

3.4.1. Radiographs

X-ray images as well as averaged radiographic scores were shown in Fig. 6. Fig. 6c showed restoration of bone defect in control group during the 12 weeks' experimental period. The 4 week image shows that the bone-resorption occurred in the middle of the bone graft because of the lack of blood support. This resorption accelerated over time. Consequently, although the bone defect was rebuilt at 12 week, but the ulna

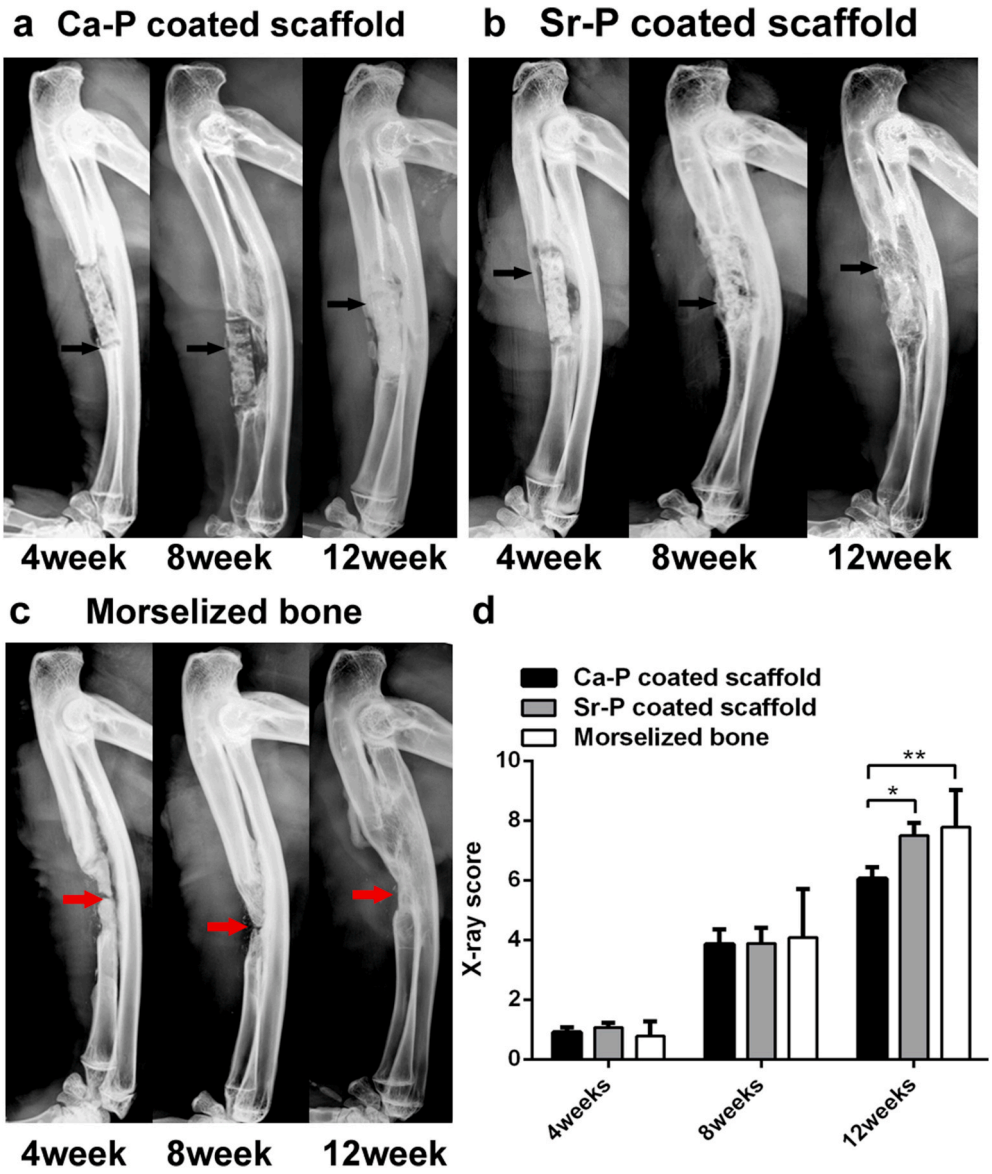

Fig. 6. X-ray images acquired in rabbit ulnae at 4, 8 and 12 weeks after implantations of Ca–P (a) and Sr–P (b) coated Mg–Sr devices and control group(c). Black arrows indicate the new bone formation and red arrows indicate the morselized bone was reabsorbed. (d) Averaged radiographic scores of Sr–P coated implants were significantly higher at 12 weeks (*p<0.05). (For interpretation of the references to color in this figure legend, the reader is referred to the Web version of this article.)

did not return to its original form. For the two coated devices, only a small amount of callus formed between the broken end of the ulna and the implantation site after 4 weeks, but the filled morselized powder was not absorbed. After 8 weeks, a bite of new bone had formed on the surface of Ca–P porous device (Fig. 6a), but the fracture line of bone defect was still obvious. In contrast, more new bone was generated and spread along the surface of the Sr–P coated porous device, and the broken line of the ulna defect appeared blurred (Fig. 6c). At 12 weeks post-surgery, bridging connections with both dense and high-density bone were apparent around the two coated implants, and the ulna regained its integrity and continuity, indicating effective healing. During the first 4 weeks, X-ray scores showed that there was no significant difference in healing between the three groups. This can be attributed to the fact that all groups were in callus formation stage, at which the main composition was newly cartilage tissue that was invisible under X-ray. Radiography eventually revealed a difference in callus morphology and size once the bone healing process entered into callus formation stage (8 weeks). Especially at 12 weeks, more new bone and substantial remodeling was evident around the Sr–P coated devices based on radiographic scores, which suggested that the extent of remodeling was significantly greater for the Sr–P–coated than the Ca–P–coated implant. Most importantly, no obvious gas accumulation was observed around all samples, indicating that two coatings can effectively increase the corrosion resistance of Mg–Sr alloy.

3.4.2. Micro-CT imaging

Representative 3D-reconstructed micro-CT images of Sr–P and Ca–P coated implants at 4, 8, and 12 weeks post-surgery are shown in Fig. 7A, to demonstrate the residual structure of implants as well as the new bone regeneration. The degradation rates shown in Fig. 7B and C were calculated based on the volume loss of devices caused by corrosion *in vivo* over time. At 4 weeks post-surgery, two coated porous devices maintained their original structure, with the device volume loss of 21 ± 2% and 15 ± 4%, respectively. Subsequently, the respective volume losses were 42 ± 4% for Sr–P coated porous devices and 29 ± 5% for Ca–P coated porous devices after 8 weeks; Especially at 12 weeks, although the volume reduction was 66 ± 5% for Sr–P coating porous device that was large than that of 42 ± 4% for Ca–P coating porous device, but the remaining implants were still partly intact, as assessed with 3D-reconstructed micro-CT imaging. The *in vivo* corrosion rate data indicated significantly greater degradation for the Sr–P coated implants compared with the Ca–P coated implants.

3.4.3. Bone mineralization

New bone mineralization around different coated devices was detected by sequential fluorescence labeling during the healing process.

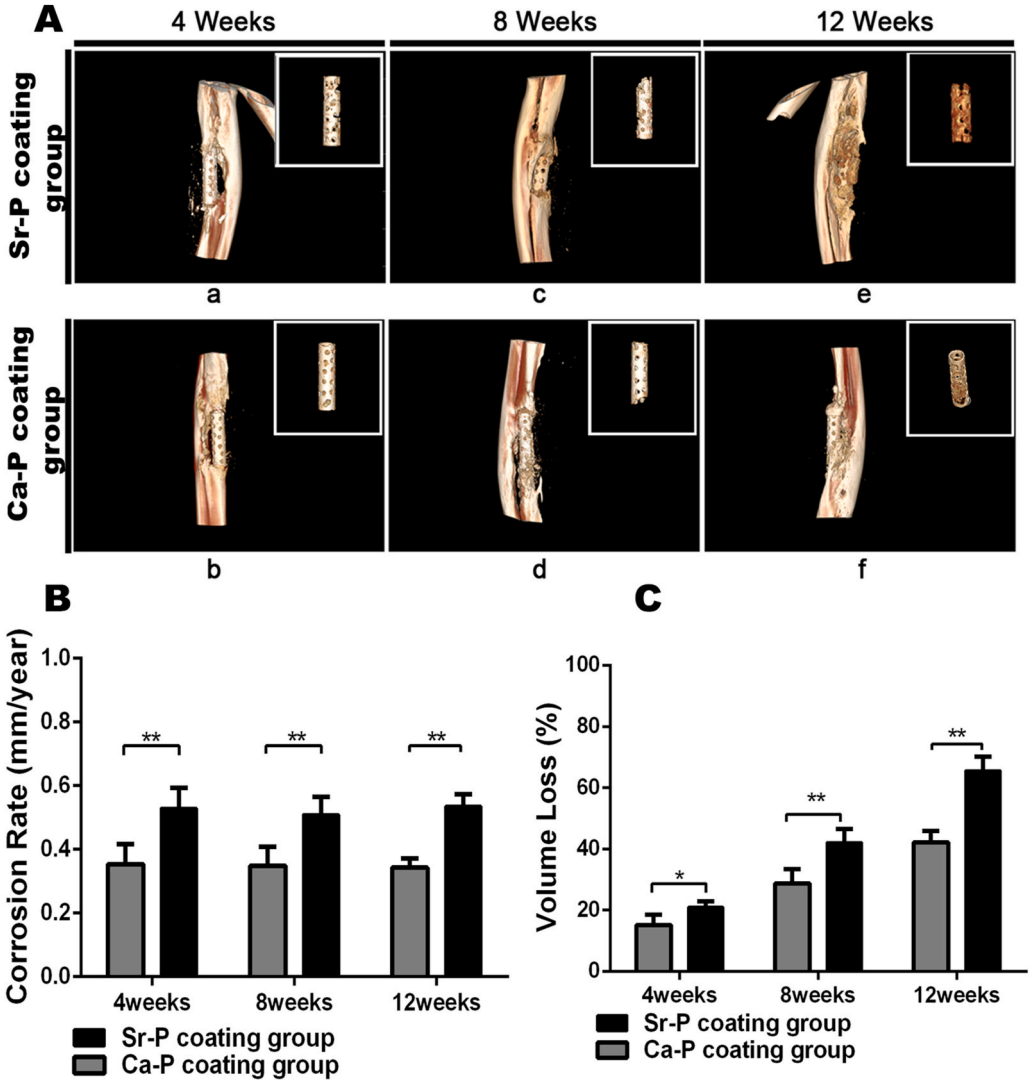

Fig. 7. A. Representative micro-CT images acquired at 4, 8 and 12 weeks: New bone formation of ulna and the morphology of the tubes after degradation. B. the corrosion rate (CR) of different coated Mg–Sr devices were calculated at 4, 8 and 12 weeks after implantation (**p‘0.01).

The area labeled with calcein, and shown in brightly green in Fig. 8A, represents the amount of new bone formation and mineral deposition. At 4 weeks post-surgery, compared with the Ca–P coated implants (new bone area = 0.4 ± 0.1 mm^2), there was greater density of fluorescence around the Sr–P coated porous devices and the area of new bone was 0.7 ± 0.1 mm^2. After 8 weeks, although the fluorescent density was enhanced around the Ca–P coating group, the intensity was still less than the Sr–P coating group. Meanwhile, the new bone area of Sr–P coated device (1.1 ± 0.3 mm^2) was still significantly greater than the Ca–P coating group (0.7 ± 0.3 mm^2); After 12 weeks, the new bone area of Sr–P coating group reached 1.3 ± 0.3 mm^2, which was significantly greater than that of the Ca–P coated devices (0.8 ± 0.2 mm^2). In addition, we must point that the newly bone area of control group was not calculated because it is difficult to clearly distinguish newly formed bone from the transplanted autogenous morselized bone.

3.4.4. Histology

It is well known that new bone formation tyles includes intramembranous ossification and endochondral ossification [37]. In addition, in mature bone tissue, osteocytes were spindle shape to arrange regularly and only a few chondrocytes are present. In contrast, in new bone tissue, the osteocytes were spherical or oval shape to arrange irregularly, and a large number of chondrocytes can be observed [38]. Therefore, it is possible to assess bone regeneration by analyzing the number of chondrocytes and the osteocytes arrangement. In present study, because of the periosteum was surgically removed in defect site, hence the bone regeneration was mainly dependent on endochondral ossification, i. e the first stage was cartilage regeneration, then the cartilage was mineralized to osteogenic tissue. Representative histological graphics were showed in Fig. 9, revealing the formation of an interface between the implant and surrounding bone tissue as well as the formation and morphology of the new bone tissue at designed time. After 4 weeks, an abundance of irregularly arranged osteocytes, matrix, and chondrocytes was observed around the implants, demonstrating active bone formation during the initial healing process. After 8 weeks, new bone tissue and chondrocytes continued to be generated around the two types of coated implants. For the Ca–P coating group, the osteocytes were more mature and arranged more regularly compared with the Sr–P coating group. After 12 weeks, the more uniform alignment of the mature osteocyte was observed surrounding the Ca–P coated porous devices, meanwhile, only limited chondrocytes were observed also confirmed this phenomenon. The Sr–P coating group had a greater number of chondrocytes and fewer mature new bone cells, which suggesting significantly enhanced chondrogenesis and more aggressive bone formation.

4. Discussion

As well known, Mg-base alloy could degraded in the simulated body fluid and caused a dynamic surface [8,10,12], which increased the difficulty of the adhesion of cells [9]. Hence, surface modification was widely used to control the degradation rate of Mg alloy to get a relatively stable surface for cell growth [14,39]. In our previous study, the surface modifications were used to improve the corrosion resistance, mechanical strength and cytocompatibility of Mg–Sr alloy matrix, and the release of beneficial ions, such as Mg^{2+}, Sr^{2+} and Ca^{2+}, from the coating and alloy matrix was observed to promote the new bone formation and help to improve the early healing process of segmental defect (only 4 weeks) [37]. Therefore, to study the balanced relationship between appropriate degradation and bioactivity of released ions on the regeneration of bone defect healing process, Sr–P coating and Ca– P coating were applied on the Mg–Sr alloy porous device. Further and deeper research to focus on mineralization and formation of new bone around the devices in segmental defect regeneration *in vivo* was studied in the present work.

According to the fitting results of *in vitro* electrochemical tests and *in vivo* corrosion rate calculated by micro-CT, the Ca–P coating illustrated greater corrosion resistance because of the double-layer structure. An MgF_2 inner-protection film was introduced by a pre-treatment in KF aqueous solution before calcium phosphate deposition, which was confirmed from the cross-sectional morphology. MgF_2 is reported to be an effective corrosion protective layer [40–42]. For example, an enhanced corrosion resistance was reported on an AZ31 scaffold by immersion and electrochemical tests [43]. The enhanced corrosion resistance eliminated the micro-galvanic couples between the Mg matrix and intermetallic phase, resulting from the encapsulation effect by MgF_2 coating. However, because the thickness of this inner layer was less than 5 μm, a long-lasting effective corrosive protection could only be achieved by the composite structure, as the case with Ca–P coating.

On the other hand, the degradation rate of Mg implants also influences ionic dissolution. For example, Mg^{2+}, Sr^{2+} and Ca^{2+} in our study. Both the direct-cultured and indirect-cultured cell assays were designed to examine the bioactive surface and the beneficial effect of released ions, respectively. The surface with high corrosion resistance is relatively stable, and attributed to the absent of dynamic fluctuation. Thus, both stable and bioactive surface can possess osteoconductive activity and therefore presents superior biological performance in the direct-cultured cell assay. While indirect contact through extraction culturing reflects the role of bioactive ionic dissolution. Many studies

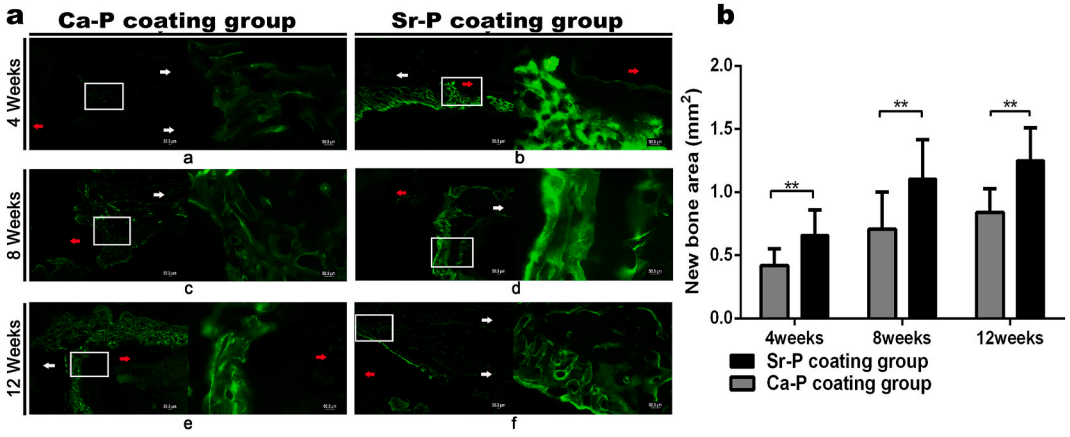

Fig. 8. A. Images of calcein green fluorescence around the device-bone interfaces at 4, 8 and 12 weeks after implantation. (a, c, e) Ca–P coated porous device. (b, d, f) Sr–P coated porous device. The fluorescence identifies sedimentary calcium and newly formed bone. Red arrows indicate the porous tubular device. White arrows indicate bone ends. In each panel, an enlargement of the area enclosed in a white square in the left image is shown on the right to indicate the new bone-mineral deposition between the implant and bone. B. The newly formed bone area of different coated Mg–Sr devices was calculated at 4, 8 and 12 weeks after implantations (**p˂0.01). (For interpretation of the references to color in this figure legend, the reader is referred to the Web version of this article.)

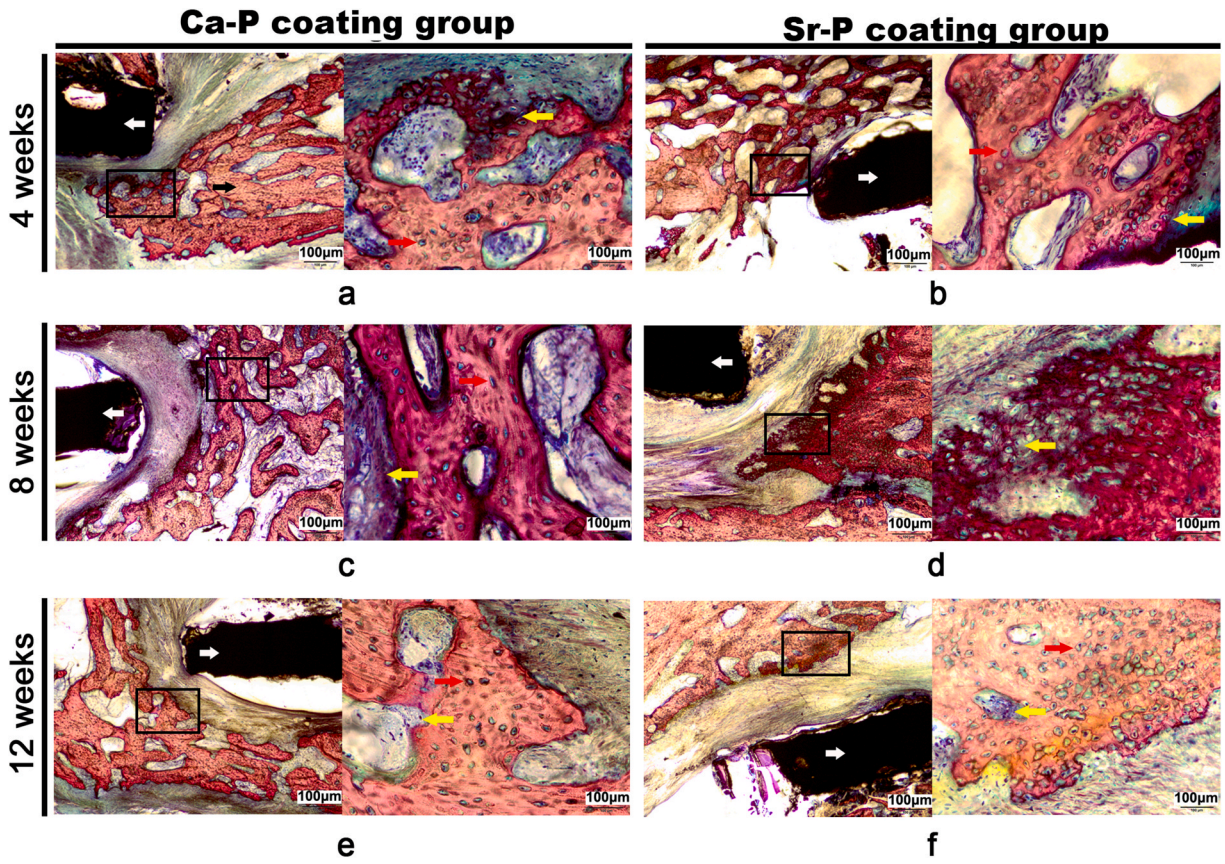

Fig. 9. Histological images of the device/bone interfaces at 4, 8 and 12 weeks after surgery. (a, c, e) Ca–P coated porous device. (b, d, f) Sr–P coated porous device. White arrows indicate the implanted device and black arrow indicate the bone end. In each panel, an enlargement of the area enclosed in a black square in the left image is shown on the right to present the new bone tissues. The yellow arrows indicate chondrocytes, which was stained blue. While red arrows indicate bone and matrix, which was stained red and mark with label red. (For interpretation of the references to color in this figure legend, the reader is referred to the Web version of this article.)

have shown that the presence of bioactive ions such as Sr, Mg, Ca, Si and Zn ions could enhance bone regeneration by means of osteoinduction [2,44,45]. From the osteogenic differentiation results in this study, the Sr–P coating presented statistically superior performance in both direct and indirect cultured cell assays than the Ca–P coating. A possible explanation is that although Sr–P coating had a higher corrosion rate than Ca–P coating, however, it was still in acceptable and controllable manner. Meanwhile, the active surface and release of ions in the case of Sr–P coating showed beneficial effect on bioactivity.

In addition, according to the radiological images *in vivo* up to 12 weeks' implantation, both the two coated porous devices with autogenous morselized bone filled showed better reconstruction and no resorption compared to the transplanted morselized bone without devices. These suggested that the resorption risk of autogenous morselized bone is effectively reduced due to the existence of implant, because the bone granules were separated from the surrounding soft tissue. Moreover, with the degradation of the Mg–Sr device, the regenerative bone callus finally can integrate with the transplanted morselized bone, such that the integrity and continuity of bone can be reconstituted. Therefore, the novel device matched the clinical application requirements, including as bone substitute [46–48] and internal fixation [49,50]. More important, in this research, we also found an interesting phenomenon. Although Ca–P coating also exhibited superior corrosion resistance *in vivo* and *in vitro*, however, the larger amount of bone regeneration and more active endochondral ossification was observed around the Sr–P coated porous device after 12 weeks. All these suggested that compared with Ca–P coating, Sr–P coating has better bone formation response.

Considering the bone defect regeneration is essentially a spreading and proliferation process with new bone tissue, so that the ideal degradation rate of biomaterial should match with the physiological healing rate [8]. In present study, our results showed that the Sr–P coating group with a relatively faster degradation rate exhibited better bone response comparing with Ca–P coating group. The reason for this phenomenon may be the overall slow degradation of Ca–P coated device limited the growth of new bone due to the space-consumed by residual porous device lead to "occupied effect". However, this was often overlooked in past decades, because most research on Mg alloy mainly focused on the improvement of corrosion resistance to reduce the hydrogen evolution [27–29,51–53]. Therefore, we believe that in the process of bone defect reconstruction, it is far from enough to just pay attention to the corrosion resistance of Mg alloy. The degradation rate should also become a problem that researchers can not ignore.

On the other hand, the release of beneficial ions (Sr^{2+}) maybe was another factor. Our results showed that higher bioactivity and more active endochondral ossification in Sr–P coating group than Ca–P coating group, which suggeated the beneficial ions to be continuously released in surrounding microenvironment in Sr–P coated porous device due to more appropriate degradation, and stimulating the body to produce more positive bone reactions. At last, we monitored serum Mg^{2+} and Ca^{2+} to avoid hypermagnesemia and pathological test of the liver, heart, brain and spleen to evaluate potential organ damage during experiment (Supporting Information Figs. S1 and S2). The result also showed that two coated devices exhibited good biosafety.

In summary, the Sr–P coating exhibited more active biological properties based on the qualitative and quantitative evaluation *in vitro* and *in vivo*, while the Ca–P coating indicated a higher corrosion

resistance. This interesting phenomenon suggests superior corrosion resistance for biodegradable Mg implants may not be the best option for critical bone defects repairing. The overall slow degradation of implants *in vivo* may cause occupied effect and limit the regeneration and remodeling of new bone during the early stage of implantation. However, a definite required degradation rate for segmental defects is also a primary problem that needs to be solved in the future. In addition, inflammation was also a problem that can not be ignored in the process of bone regeneration [54–56]. Although our results did not showed an obvious inflammatory response, but it should be focused in future research. What's more, as the trial time of 3 months is relatively short, a long-term study should be undertaken to verify the effect of degradation and biological properties on the segmental defect regeneration.

5. Conclusions

Novel hollow magnesium-strontium (Mg–Sr) tubular devices were fabricated and modificated using designed coatings (Sr–P and Ca–P), considering the degradation rate and biological properties, with autogenous morselized bone filled to address the challenges in segmental defects regeneration. The two coated groups indicated an effective healing after 12 weeks implantation. Moreover, Sr–P coated implants possessed appropriate degradation rate, in addition to, dual biological function of bioactive surface and ionic dissolution, indicated its promising application in segmental defects regeneration.

CRediT authorship contribution statement

Nan Zhang: Conceptualization, Methodology, Validation, Formal analysis, Investigation, Funding acquisition, Writing - original draft, Writing - review & editing. **Weidan Wang:** Conceptualization, Methodology, Validation, Software, Formal analysis, Investigation, Writing - original draft, Writing - review & editing. **Xiuzhi Zhang:** Writing - review & editing, Formal analysis. **Krishna. C. Nune:** Methodology, Formal analysis. **Ying Zhao:** Investigation, Data curation. **Na Liu:** Methodology, Visualization, Software. **R.D.K. Misra:** Resources, Writing - review & editing. **Ke Yang:** Supervision, Project administration, Writing - review & editing. **Lili Tan:** Supervision, Project administration, Conceptualization, Funding acquisition, Writing - review & editing. **Jinglong Yan:** Supervision, Project administration, Conceptualization, Funding acquisition, Writing - review & editing.

Declaration of competing interest

All authors declared that no conflict of interest exits in the submission of this manuscript, and manuscript was approved by all authors for publication. I would like to declare on behalf of my co-authors that the work described was original research that has not been published previously, and not under consideration for publication elsewhere, in whole or in part. All the authors listed have approved the manuscript that is enclosed.

Acknowledgements

This work was financially supported by funds from Basic Research Project from the Education Office of Heilongjiang Province (2017-KYYWF-0738), Key Program of China on Biomedical Materials Research and Tissue and Organ Replacement (No. 2016YFC1101804, 2016YFC1100604), Institute of Metal Research, Chinese Academy of Sciences (No.2015-ZD01), and National Natural Science Foundation of China (No.31500777 and 81472107). Authors also thank the Department of Metallurgical, Materials and Biomedical Engineering of the University of Texas at EI Paso, for providing laboratory facilities for the cell culture experiments.

Appendix A. Supplementary data

Supplementary data to this article can be found online at https://doi.org/10.1016/j.bioactmat.2020.11.026.

References

[1] P. Kasten, J. Vogel, F. Geiger, P. Niemeyer, R. Luginbühl, K. Szalay, The effect of platelet-rich plasma on healing in critical-size long-bone defects, Biomaterials 29 (29) (2008) 3983–3992.
[2] E. O'Neill, G. Awale, L. Daneshmandi, O. Umerah, K.W.-H. Lo, The roles of ions on bone regeneration, Drug Discov. Today 23 (4) (2018) 879–890.
[3] C.T. Laurencin, L.S. Nair, Regenerative engineering: approaches to limb regeneration and other grand challenges, Regenerative engineering and translational medicine 1 (1–4) (2015) 1–3.
[4] K.W. Lo, K.M. Ashe, H.M. Kan, C.T. Laurencin, The role of small molecules in musculoskeletal regeneration, Regen. Med. 7 (4) (2012) 535–549.
[5] M.F. Swiontkowski, H.T. Aro, S. Donell, J.L. Esterhai, J. Goulet, A. Jones, P. J. Kregor, L. Nordsletten, G. Paiement, A. Patel, Recombinant human bone morphogenetic protein-2 in open tibial fractures: a subgroup analysis of data combined from two prospective randomized studies, J Bone Joint Surg Am 88 (6) (2006) 1258–1265.
[6] J.A. Cobos, R.W. Lindsey, Z. Gugala, The cylindrical titanium mesh cage for treatment of a long bone segmental defect: description of a new technique and report of two cases, J. Orthop. Trauma 14 (1) (2000) 54–59.
[7] J. Nagels, M. Stokdijk, P.M. Rozing, Stress shielding and bone resorption in shoulder arthroplasty, J. Shoulder Elbow Surg. 12 (1) (2003) 35–39.
[8] M.P. Staiger, A.M. Pietak, J. Huadmai, G. Dias, Magnesium and its alloys as orthopedic biomaterials: a review, Biomaterials 27 (9) (2006) 1728–1734.
[9] L. Mao, L. Shen, J. Chen, Y. Wu, M. Kwak, Y. Lu, Q. Xue, J. Pei, L. Zhang, G. Yuan, Enhanced bioactivity of Mg–Nd–Zn–Zr alloy achieved with nanoscale MgF2 surface for vascular stent application, ACS Appl. Mater. Interfaces 7 (9) (2015) 5320–5330.
[10] J. Han, P. Wan, Y. Ge, X. Fan, L. Tan, J. Li, K. Yang, Tailoring the degradation and biological response of a magnesium–strontium alloy for potential bone substitute application, Mater. Sci. Eng. C 58 (2016) 799–811.
[11] Z. Zhai, X. Qu, H. Li, K. Yang, P. Wan, L. Tan, Z. Ouyang, X. Liu, B. Tian, F. Xiao, The effect of metallic magnesium degradation products on osteoclast-induced osteolysis and attenuation of NF-κB and NFATc1 signaling, Biomaterials 35 (24) (2014) 6299–6310.
[12] F. Witte, V. Kaese, H. Haferkamp, E. Switzer, A. Meyer-Lindenberg, C. Wirth, H. Windhagen, In vivo corrosion of four magnesium alloys and the associated bone response, Biomaterials 26 (17) (2005) 3557–3563.
[13] S. Chen, S. Guan, W. Li, H. Wang, J. Chen, Y. Wang, In vivo degradation and bone response of a composite coating on Mg-Zn-Ca alloy prepared by microarc oxidation and electrochemical deposition, *J Biomed Mater Res B Appl Biomater*100 (2) (2012) 533–543.
[14] M. Li, X. Yang, W. Wang, Y. Zhang, P. Wan, K. Yang, Y. Han, Evaluation of the osteo-inductive potential of hollow three-dimensional magnesium-strontium substitutes for the bone grafting application, Mater. Sci. Eng. C 73 (2017) 347–356.
[15] M. Li, W. Wang, Y. Zhu, Y. Lu, P. Wan, K. Yang, Y. Zhang, C. Mao, Molecular and cellular mechanisms for zoledronic acid-loaded magnesium-strontium alloys to inhibit giant cell tumors of bone, Acta Biomater. 1 (77) (2018) 365–379.
[16] C.J. Chung, H.Y. Long, Systematic strontium substitution in hydroxyapatite coatings on titanium via micro-arc treatment and their osteoblast/osteoclast responses, Acta Biomater. 7 (11) (2011) 4081–4087.
[17] M. Li, P. He, Y. Wu, Y. Zhang, H. Xia, Y. Zheng, Y. Han, Stimulatory effects of the degradation products from Mg-Ca-Sr alloy on the osteogenesis through regulating ERK signaling pathway, Sci. Rep. 6 (2016) 32323.
[18] Z. Saidak, P.J. Marie, Strontium signaling: Molecular mechanisms and therapeutic implications in osteoporosis, Pharmacol. Ther. 136 (2012) 216–226.
[19] W. Zhang, Y. Tian, H. He, R. Chen, Y. Ma, H. Guo, Y. Yuan, C. Liu, Strontium attenuates rhBMP-2-induced osteogenic differentiation via formation of Sr-rhBMP-2 complex and suppression of Smad-dependent signaling pathway, Acta Biomater. 33 (2016) 290–300.
[20] E. Boanini, P. Torricelli, M. Gazzano, E. Della Bella, M. Fini, A. Bigi, Combined effect of strontium and zoledronate on hydroxyapatite structure and bone cell responses, Biomaterials 35 (2014) 5619–5626.
[21] X. Chen, D. Nisbet, R. Li, P. Smith, T. Abbott, M. Easton, D.-H. Zhang, N. Birbilis, Controlling initial biodegradation of magnesium by a biocompatible strontium phosphate conversion coating, Acta Biomater. 10 (3) (2014) 1463–1474.
[22] J. Niu, G. Yuan, Y. Liao, L. Mao, J. Zhang, Y. Wang, F. Huang, Y. Jiang, Y. He, W. Ding, Enhanced biocorrosion resistance and biocompatibility of degradable Mg–Nd–Zn–Zr alloy by brushite coating, Mater. Sci. Eng. C 33 (8) (2013) 4833–4841.
[23] 10993-5 E. ISO, Biological Evaluation of Medical Devices. Part 5: Tests for in Vitro Cytotoxicity, International Organization for Standardization, Geneva, Switzerland, 2009.
[24] Y.X. Sun, C.L. Sun, Y. Tian, W.X. Xu, C.L. Zhou, C.Y. Xi, J.L. Yan, X.T. Wang, A comparison of osteocyte bioactivity in fine particulate bone powder grafts vs larger bone grafts in a rat bone repair model, Acta Histochem. 116 (6) (2014) 1015–1021.
[25] Z. Xi, Y. Wu, S. Xiang, C. Sun, Y. Wang, H. Yu, Y. Fu, X. Wang, J. Yan, D. Zhao, Y. Wang, N. Zhang, Corrosion resistance and biocompatibility assessment of a

biodegradable hydrothermal-coated Mg−Zn−Ca alloy: an in vitro and in vivo study, ACS Omega 5 (9) (2020) 4548–4557.
[26] N. Zhang, D. Zhao, N. Liu, Y. Wu, J. Yang, Y. Wang, H. Xie, Y. Ji, C. Zhou, J. Zhuang, Assessment of the degradation rates and effectiveness of different coated Mg-Zn-Ca alloy scaffolds for in vivo repair of critical-size bone defects, J. Mater. Sci. Mater. Med. 29 (9) (2018) 138.
[27] F. Witte, J. Fischer, J. Nellesen, C. Vogt, J. Vogt, T. Donath, F. Beckmann, In vivo corrosion and corrosion protection of magnesium alloy LAE442, Acta Biomater. 6 (5) (2010) 1792–1799.
[28] P. Jiang, C. Blawert, R. Hou, N. Scharnagl, J. Bohlen, M. Zheludkevich, Microstructural influence on corrosion behavior of Mg Zn Ge alloy in NaCl solution, J. Alloys Compd. 783 (30) (2019) 179–192.
[29] D. Gandel, N. Birbilis, M.A. Easton, M. Gibson, Influence of manganese, zirconium and iron on the corrosion of magnesium, Proc. Corros. Prev. (2010) 875–885.
[30] P. Jiang, C. Blawert, N. Scharnagl, M. Zheludkevich, Influence of water purity on the corrosion behavior of Mg0.5ZnX (X= Ca, Ge) alloys, Corrosion Sci. 153 (2019) 62–73.
[31] J. Li, L. Tan, P. Wan, et al., Study on microstructure and properties of extruded Mg–2Nd–0.2 Zn alloy as potential biodegradable implant material, Mater. Sci. Eng. C 49 (2015) 422–429.
[32] X.N. Gu, N. Li, Y.F. Zheng, L.Q. Ruan, In vitro degradation performance and biological response of a Mg–Zn–Zr alloy, Mater. Sci. Eng., B 176 (20) (2011) 1778–1784.
[33] J. Han, P. Wan, Y. Sun, Z. Liu, X. Fan, L. Tan, K. Yang, Fabrication and evaluation of a bioactive Sr–Ca–P contained micro-arc oxidation coating on magnesium strontium alloy for bone repair application, J. Mater. Sci. Technol. 32 (3) (2016) 233–244.
[34] S.S. Kim, C.A. Sundback, S. Kaihara, M.S. Benvenuto, B.-S. Kim, D.J. Mooney, J. P. Vacanti, Dynamic seeding and in vitro culture of hepatocytes in a flow perfusion system, Tissue Eng. 6 (1) (2000) 39–44.
[35] K. Yamamoto, T. Kishida, Y. Sato, et al., Direct conversion of human fibroblasts into functional osteoblasts by defined factors, Proc. Natl. Acad. Sci. Unit. States Am. 112 (19) (2015) 6152–6157.
[36] E.R. Balmayor, J.P. Geiger, M.K. Aneja, T. Berezhanskyy, M. Utzinger, O. Mykhaylyk, C. Rudolph, C. Plank, Chemically modified RNA induces osteogenesis of stem cells and human tissue explants as well as accelerates bone healing in rats, Biomaterials 87 (2016) 131–146.
[37] W. Wang, K.C. Nune, L. Tan, N. Zhang, J. Dong, J. Yan, R.D.K. Misra, K. Yang, Bone regeneration of hollow tubular magnesium-strontium scaffolds in critical-size segmental defects: effect of surface coatings, Mater. Sci. Eng. C 2 (2019) 67.
[38] R.J. Hinton, Y. Jing, J. Jing, J.Q. Feng, Roles of chondrocytes in endochondral bone formation and fracture repair, J. Dent. Res. 96 (1) (2017) 23–30.
[39] C. Liu, P. Wan, L.L. Tan, K. Wang, K. Yang, Preclinical investigation of an innovative magnesium-based bone graft substitute for potential orthopaedic applications, Journal of Orthopaedic Translation 2 (3) (2014) 139–148.
[40] T. Yan, L. Tan, D. Xiong, X. Liu, B. Zhang, K. Yang, Fluoride treatment and in vitro corrosion behavior of an AZ31B magnesium alloy, Mater. Sci. Eng. C 30 (5) (2010) 740–748.
[41] X. Lin, L. Tan, P. Wan, X. Yu, K. Yang, Z. Hu, Y. Li, W. Li, Characterization of micro-arc oxidation coating post-treated by hydrofluoric acid on biodegradable ZK60 magnesium alloy, Surf. Coating. Technol. 232 (2013) 899–905.
[42] J. Trinidad, G. Arruebarrena, I. Marco, I. Hurtado, E. Sáenz de Argandoña, Effectivity of fluoride treatment on hydrogen and corrosion product generation in temporal implants for different magnesium alloys, Proc. IME H J. Eng. Med. 227 (12) (2013) 1301–1311.
[43] W. Yu, H. Zhao, Z. Ding, Z. Zhang, B. Sun, J. Shen, S. Chen, B. Zhang, K. Yang, M. Liu, In vitro and in vivo evaluation of MgF2 coated AZ31 magnesium alloy porous scaffolds for bone regeneration, Colloids Surf. B Biointerfaces 149 (2017) 330–340.
[44] G.M. Kuang, W. Yau, J. Wu, K.W. Yeung, H. Pan, W. Lam, W. Lu, K. Chiu, Strontium exerts dual effects on calcium phosphate cement: accelerating the degradation and enhancing the osteoconductivity both in vitro and in vivo, J. Biomed. Mater. Res. 103 (5) (2015) 1613–1621.
[45] L. Mao, L. Xia, J. Chang, J. Liu, L. Jiang, C. Wu, B. Fang, The synergistic effects of Sr and Si bioactive ions on osteogenesis, osteoclastogenesis and angiogenesis for osteoporotic bone regeneration, Acta Biomater. 61 (2017) 217–232.
[46] K. Bobe, E. Willbold, I. Morgenthal, O. Andersen, T. Studnitzky, J. Nellesen, W. Tillmann, C. Vogt, K. Vano, F. Witte, In vitro and in vivo evaluation of biodegradable, open-porous scaffolds made of sintered magnesium W4 short fibres, Acta Biomater. 9 (10) (2013) 8611–8623.
[47] S. Singh, P. Vashisth, A. Shrivastav, N. Bhatnagar, Synthesis and characterization of a novel open cellular Mg-based scaffold for tissue engineering application, J Mech Behav Biomed Mater 94 (19) (2019) 54–62.
[48] Y. Li, J. Zhou, P. Pavanram, M.A. Leeflang, L.I. Fockaert, B. Pouran, N. Tümer, K. U. Schröder, J. Mol, H. Weinans, H. Jahr, A.A. Zadpoor, Additively manufactured biodegradable porous magnesium, Acta Biomater. 67 (2018) 378–392.
[49] D. Zhao, S. Huang, F. Lu, B. Wang, L. Yang, L. Qin, K. Yang, Y. Li, W. Li, W. Wang, S. Tian, X. Zhang, W. Gao, Z. Wang, Y. Zhang, X. Xie, J. Wang, J. Li, Vascularized bone grafting fixed by biodegradable magnesium screw for treating osteonecrosis of the femoral head, Biomaterials 81 (3) (2016) 84–92.
[50] A. Chaya, S. Yoshizawa, K. Verdelis, S. Noorani, B.J. Costello, C. Sfeir, Fracture healing using degradable magnesium fixation plates and screws, J. Oral Maxillofac. Surg. 73 (2) (2015) 295–305.
[51] K. Jähn, H. Saito, H. Taipaleenmäki, A. Gasser, N. Hort, F. Feyerabend, H. Schlüter, J.M. Rueger, W. Lehmann, R. Willumeit-Römer, E. Hesse, Intramedullary Mg_2Ag nails augment callus formation during fracture healing in mice, Acta Biomater. 36 (2016) 350–360.
[52] W. Wang, P. Wan, C. Liu, L. Tan, W. Li, L. Li, K. Yang, Degradation and biological properties of Ca-P contained micro-arc oxidation self-sealing coating on pure magnesium for bone fixation, Regenerative biomaterials 2 (2) (2014) 107–118.
[53] J. Zhuang, Y. Jing, Y. Wang, J. Zhang, H. Xie, J. Yan, Degraded and osteogenic properties of coated magnesium alloy AZ31; an experimental study, J. Orthop. Surg. Res. 11 (2016) 30.
[54] H. Chen, J. Erndt-Marino, P. Diaz-Rodriguez, Jonathan Kulwatno, Andrea C. Jimenez-Vergara, Susan L. Thibeault, Mariah S. Hahn, In vitro evaluation of anti-fibrotic effects of select cytokines for vocal fold scar treatment, J. Biomed. Mater. Res. B Appl. Biomater. 107 (4) (2019) 1056–1067.
[55] L. Sun, X. Li, M. Xu, F. Yang, W. Wang, X. Niu, In vitro immunomodulation of magnesium on monocytic cell toward anti-inflammatory macrophages, Regen Biomater 7 (4) (2020) 391–401.
[56] Patricia Diaz-Rodriguez, Hongyu Chen, D. Joshua, Erndt-Marino, Fei Liu, Filbert Totsingan, Richard A. Gross, Mariah S. Hahn, Impact of select sophorolipid derivatives on macrophage polarization and viability, ACS Appl. Bio Mater 2 (1) (2019) 601–612.